HAL
open science

Development of a multi-functional preclinical device for the treatment of glioblastoma

Khaled Metwally, Chiara Bastiancich, Florian Correard, Anthony Novell, Samantha Fernandez, Benjamin Guillet, Benoit Larrat, Serge Mensah, Marie-Anne Estève, Anabela da Silva

To cite this version:

Khaled Metwally, Chiara Bastiancich, Florian Correard, Anthony Novell, Samantha Fernandez, et al.. Development of a multi-functional preclinical device for the treatment of glioblastoma. Biomedical optics express, 2021, 12 (4), pp.2264-2279. 10.1364/boe.419412 . hal-03248327

HAL Id: hal-03248327

https://hal.science/hal-03248327v1

Submitted on 3 Jun 2021

HAL is a multi-disciplinary open access archive for the deposit and dissemination of scientific research documents, whether they are published or not. The documents may come from teaching and research institutions in France or abroad, or from public or private research centers.

L'archive ouverte pluridisciplinaire **HAL**, est destinée au dépôt et à la diffusion de documents scientifiques de niveau recherche, publiés ou non, émanant des établissements d'enseignement et de recherche français ou étrangers, des laboratoires publics ou privés.

Research Article Vol. 12, No. 4 / 1 April 2021 / Biomedical Optics Express 2264

Biomedical Optics EXPRESS

Development of a multi-functional preclinical device for the treatment of glioblastoma

KHALED METWALLY,[1,2,9] CHIARA BASTIANCICH,[3,9] FLORIAN CORREARD,[3,4] ANTHONY NOVELL,[5] SAMANTHA FERNANDEZ,[6] BENJAMIN GUILLET,[6,7] BENOIT LARRAT,[8] SERGE MENSAH,[2] MARIE-ANNE ESTÈVE,[3,4] AND ANABELA DA SILVA[1,*]

[1]*Aix Marseille Univ, CNRS, Centrale Marseille, Institut Fresnel, Marseille, France*
[2]*Aix Marseille Univ, CNRS, Centrale Marseille, LMA, Marseille, France*
[3]*Aix Marseille Univ, CNRS, INP, Inst Neurophysiopathol, Marseille, France*
[4]*APHM, Hôpital de la Timone, Service Pharmacie, Marseille, France*
[5]*Université Paris-Saclay, CEA, CNRS, Inserm, BioMaps, Service Hospitalier Frédéric Joliot, Orsay, France*
[6]*Aix-Marseille Univ, Centre Européen de Recherche en Imagerie Médicale (CERIMED), Marseille, France*
[7]*Aix-Marseille Univ, INSERM, INRA, Center de Recherche en Cardiovasculaire et Nutrition (C2VN), Marseille, France*
[8]*Univ. Paris Saclay, CNRS, CEA, DRF/JOLIOT/NEUROSPIN/BAOBAB, Gif-sur-Yvette, France*
[9]*Contributed equally to this work*
[*]*anabela.dasilva@fresnel.fr*

Abstract: Glioblastoma multiforme (GBM) is one of the most common and aggressive malignant primary brain tumors in adults. The treatment of GBM is limited by the blood-brain barrier (BBB), which limits the diffusion of appropriate concentrations of therapeutic agents at the tumor site. Among experimental therapies, photo-thermal therapy (PTT) mediated by nanoparticles is a promising strategy. To propose a preclinical versatile research instrument for the development of new PTT for GBM, a multipurpose integrated preclinical device was developed. The setup is able to perform: i) BBB permeabilization by focused ultrasound sonication (FUS); ii) PTT with continuous wave laser; iii) *in situ* temperature monitoring with photo-acoustic (PA) measurements. *In vivo* preliminary subcutaneous and transcranial experiments were conducted on healthy or tumor-bearing mice. Transcranial FUS-induced BBB permeabilization was validated using single photon emission computed tomography (SPECT) imaging. PTT capacities were monitored by PA thermometry, and are illustrated through subcutaneous and transcranial *in vivo* experiments. The results show the therapeutic possibilities and ergonomy of such integrated device as a tool for the validation of future treatments.

© 2021 Optical Society of America under the terms of the OSA Open Access Publishing Agreement

1. Introduction

Glioblastoma multiforme (GBM) is one of the most common and aggressive malignant brain tumors in adults. Current standard of care therapies, consisting in surgery followed by radiotherapy and chemotherapy, are ineffective and GBM currently remains incurable due to multiple factors such as high invasiveness, chemoresistance and high tendency to form recurrences [1–3]. For these reasons, there is an urgent need to find novel and efficient therapeutic strategies for this tumor.

One major limiting factor for brain tumors chemotherapies is the Blood-Brain Barrier (BBB), which prevents drugs from spreading from the vascular network to the central nervous system (CNS) limiting their penetration at the tumor site. To circumvent the BBB and enhance drug delivery into the CNS, three main strategies are currently being evaluated: (i) the development of nanomedicines sufficiently small to cross the BBB by passive targeting or grafted with peptides to bypass the BBB by active targeting [4]; (ii) the local drug delivery into the brain (*e.g.* direct

#419412 https://doi.org/10.1364/BOE.419412
Journal © 2021 Received 8 Jan 2021; revised 11 Mar 2021; accepted 12 Mar 2021; published 23 Mar 2021

Biomedical Optics EXPRESS

intracranial administration or convection-enhanced delivery) [5]; and (iii) the use of Focused Ultrasound Sonication (FUS) combined with intravascular microbubbles [6].

This last strategy seems promising as it allows the localized permeabilization of the BBB by combining focused ultrasound with intravenously injected microbubbles [7]. These gas-filled 1-5 μm microbubbles (commercially available as contrast agents *e.g.* Sonovue, Optison, Definity) can repeatedly expand and compress upon exposure to low acoustic pressures (stable cavitation), leading to tight junctions opening *via* mechanical stress on the endothelium. These rapid expansions and contractions can also create micro-streams able to disrupt the endothelial lining by shear stress [6]. This technique has been recently shown to be well-tolerated and transient in GBM patients [8], although its efficacy in increasing drug delivery into the brain has not been shown in clinical trials yet.

Alternative anti-GBM therapies, combined with conventional treatment modalities (*e.g.* ionizing radiation, chemotherapy, surgical treatment or immunotherapy), also involve multiphysical processes inducing apoptosis, among which Photo-Dynamic Therapy (PDT) or hyperthermia, or even localized tumor ablation.

Hyperthermia is a long-standing therapy to treat tumors and destroy the malignant cells in a non-chemical manner [9,10]. It consists of raising the temperature of tumor-loaded tissue to 41-50°C (or even higher) for a period that varies from few minutes to hours, using a heating source that can be HIFU (High Intensity Focused Ultrasound) or electromagnetic source in the microwave or optical wavelength range. In the latter case, the therapy is also known as Laser-Induced Thermo-Therapy (LITT) or Photo-Thermal Therapy (PTT) and usually utilizes Continuous Wave (CW) lasers in the Near-Infrared (NIR) spectrum in order to penetrate reasonable depths in the tissues. PTT localized hyperthermia reduces the potential to cause adverse effects in other organs than the targeted one leading to a safer and more efficient treatment.

As an attempt to improve heating performances and localization of the therapy, metallic nanoparticles (NPs) have emerged as potential photoabsorbing agents for PTT [11,12]. Ideal photoabsorbing agents should be non toxic in absence of laser exposure and should have strong absorption coefficient in the therapeutic window (red to near-infrared 600-1000 nm) for deep penetration through soft tissues. Good photoabsorbers are either metallic NPs that can be tuned to have plasmon resonance in the NIR spectrum by varying their size and geometry, or polymeric nanocarriers incorporating photothermal agents (*e.g.* IR-780) [13]. Several NPs have proven PTT efficacy against brain tumors, *in vitro* or *in vivo*, including gold NPs [14–17], copper sulfide nanocages [18], carbon-based nanomaterials [19–21] or donor-acceptor conjugated polymeric NPs [22,23]. Recently, laser-synthesized Titanium Nitride NPs (TiN NPs) have proven as new candidates [24,25], for which we have demonstrated *in vitro* (U87-MG GBM cell cultures) a low cytotoxicity combined with a good cellular uptake and PTT effect. Different *in vitro* and *in vivo* studies have demonstrated the interest of PTT in GBM treatment.

Regardless of the physical heating process, the treatment also requires a thermometry system to measure the temperature evolution and a control console for dosing hyperthermia. Monitoring the temperature inside the tumor is one of the biggest challenges. Many methods for non-invasive and real time temperature monitoring while executing the treatment are under investigation. Infrared thermography is limited to surface measurements. Magnetic resonance imaging (MRI), US and Computed Tomography (CT)-based thermography methods are non-invasive and contactless but not widely available (MRI, CT) or lack accuracy (US). Photoacoustic (PA) imaging has proven to be a good candidate for monitoring the temperature in real-time, *in situ* and in depth [26–29]. Being inherently multiphysical, the PA signal is sensitive to both optical and acoustic contrasts, and hence to any thermodynamic variation. Temperature-induced changes in the PA signal amplitude allows a fast and local monitoring of the temperature variations. The ergonomy of the instrumentation used (optical fibers, transducers) allows a flexible combination with PTT. Furthermore, the time-resolved PA signal can detect deeply embedded tumors based on the optical

Biomedical Optics EXPRESS

contrast between cancerous and healthy tissue. Enhanced by the presence of photoabsorbers in the tumor, PA imaging can furthermore aid in identifying cancerous lesions.

In the present paper, we propose a novel preclinical integrated device that allows performing on the same bench BBB opening with confocal FUS to improve local accumulation of NPs at the tumor site, highly localized PTT and non-invasive *in situ* PA thermometry. Several setups have been proposed in the past for a joint PTT and PA temperature measurement within different geometries, however without combination with BBB disruption system [26–29]. In some cases, the heating source and acoustic detector are positioned in transmission measurement [30,31], or orthogonally [32]. Beyond monitoring, some setups are also able to perform a real 3D thermography [33,34], with tomographic measurements. These kinds of setups are not compatible with GBM PTT that requires epi-detection. Other setups that satisfy this requirement have been alternatively proposed using a conical lens with a drilled hole in its center for receiving a transducer [35–37] or, conversely, a specifically manufactured transducer pierced in its center to allow a combination with optical irradiation [28]. The former epi-detection combination has been used with a separate BBB opening by FUS [38,39]. Recently, Kim *et al.* [40] have shown an advanced integrated setup capable of performing PTT with FUS and PA temperature monitoring, without BBB opening. Furthermore, in order to promote the accumulation of the NPs in the tumor, a beforehand reversible BBB opening strategy using FUS induced stable cavitation of microbubbles was implemented [41]. Very recently, Assi *et al.* reported the possibility of real-time temperature monitoring and control of NP-mediated thermal therapy in *ex vivo* tissue, using commercial PA imaging system (Vevo LAZR, FUJIFILM VisualSonics) equipped with 21 MHz ultrasound transducer and a nanosecond excitation laser [42]. To the best of our knowledge, no fully integrated setup that combines BBB opening with FUS, PTT and PA temperature monitoring has been reported so far in animals, although the possibility of such a development has been mentioned as possible perspectives by some authors (*e.g.* [38]).

The next section presents the fully integrated device that we have developed. To demonstrate that the different features of this device are fully operational, we performed preliminary proof-of-concept *in vivo* studies. The FUS-BBB opening, performed on healthy mice, was confirmed by Single Photon Emission Computed Tomography (SPECT) imaging, and described in section 3.1. The feasibility of the simultaneous PTT and PA thermometry, conducted on mice with subcutaneously grafted glioblastoma tumors, is also described in sections 3.2 and 3.3. Finally, a proof-of-concept experiment on a mouse bearing an orthotopically-grafted brain tumor is also presented in section 3.4.

2. Materials and methods

In this section are described the design of the multipurpose device, the principles of PTT monitored by PA thermometry, the experimental procedures and protocols of the *in vivo* experiments.

2.1. Description of the integrated device

A schema of the developed multi-functional setup is presented in Fig. 1.

The device can be decomposed into three parts:

- The FUS/PTT/PA probe (Fig. 1, Bottom) comprises a single-element focused transducer (diameter 25 mm, focal depth 20±2 mm, central frequency 1.5 MHz, Imasonic, France), presenting a hole in its center (diameter of central hole 6 mm, specifically manufactured by Imasonic, France). The measured focal volume of the transducer was 1×1×6 mm^3 at −6 dB. The output pressure of the transducer were measured in a degassed water tank, using a 0.5 mm needle hydrophone (Precision Acoustics, Dorchester, UK) mounted on a positioning stage. The transducer was driven by a built-in signal generator connected *via* a 20 W power amplifier (Image Guided Therapy, France) (Fig. 2). The acquired signal from the hydrophone was sampled by the oscilloscope (Picoscope 5243A, Pico Technology, UK). After scanning the whole focal spot, the hydrophone

Biomedical Optics EXPRESS

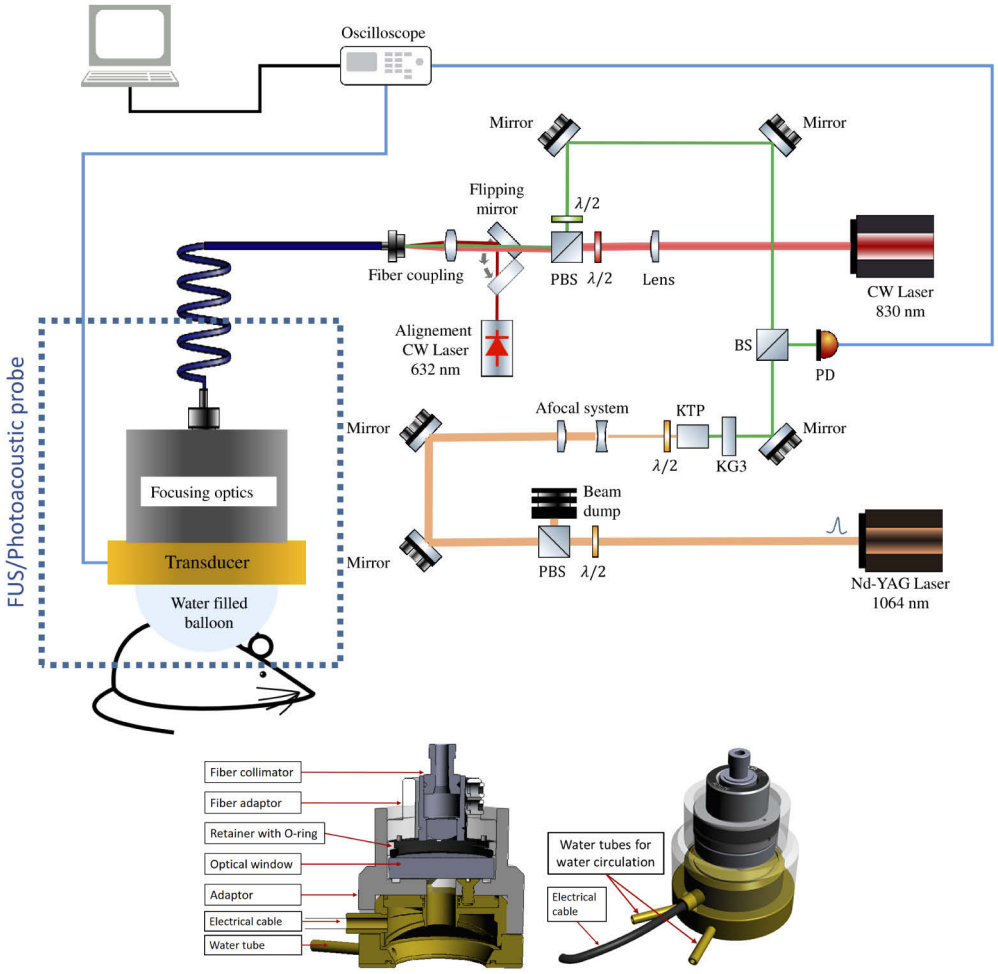

Fig. 1. *Top*: Schema of the integrated experimental setup (PBS: Polarizing beam splitter; BS: Beam sampler; KTP: Frequency doubling KTP crystal; KG3: Filter glass (Bandpass: 315 - 710 nm); PD: Si Photodetector (Detector, 200 - 1100 nm); $\lambda/2$: Achromatic half-wave plate). *Bottom*: Cross-section (*left*) and 3D view (*right*) of the FUS/PTT/PA probe.

Biomedical Optics EXPRESS

was placed in the center on the focal spot to record the relationship between the electrical input and acoustic pressure. The ultrasound transducer was then coupled to the head of the animal *via* the water balloon filled with deionized and degassed water to reach 7 to 10 mm thickness, depending on the targeted depth, and covered with degassed echographic gel (70% v/v in water). Electrical power sent to the transducer was monitored during the BBB opening session. As a coupling medium, a thin and transparent latex-based membrane was fixed to the transducer and a water filling circuit was connected in order to fill or empty this balloon up to the desired thickness. This flexibility permits a scanning in depth up to 13±2 mm of the examined organ. The water was degassed with built-in pumps in order to avoid any acoustic impedance mismatch within the balloon. The hermeticity is guaranteed by an O-ring. The transducer can be used in two modes: active mode as emitter for the BBB opening with FUS, or passive mode as receiver for the temperature monitoring with PA. The PA signal is collected through a digital oscilloscope (Picoscope 5243A, 2 channels, 100 MHz, 500 MSamples/s, rise time 5.8 ns, Pico Technology, UK). A hermetic glass window has been mounted and positioned on the top of the transducer mount in order to receive an optical fiber (MHP910L02, Core Ø910 μm, 0.22 NA, Thorlabs, Germany) through which the light sources are delivered to the sample.

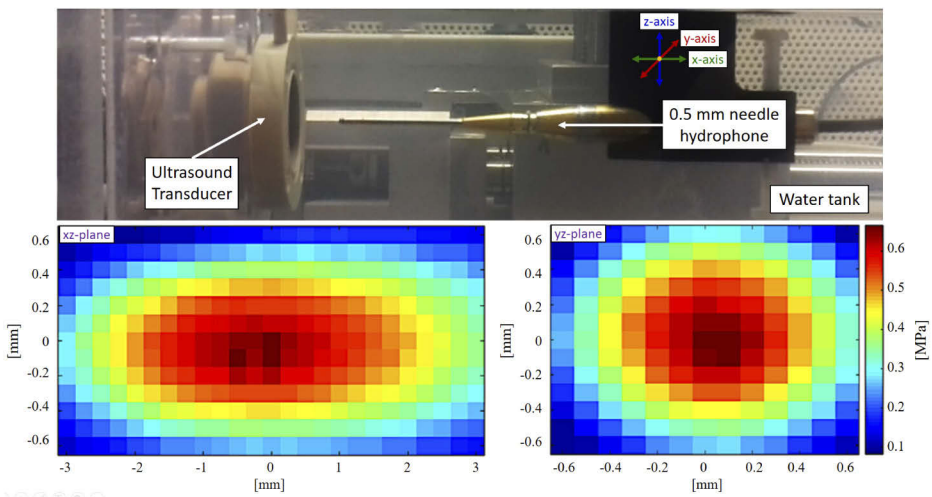

Fig. 2. Calibration of ultrasound transducer. *Top*: Experimental setup *Bottom left*: axial slice view of the focal spot. *Bottom right*: cross-section view of the focal spot, measurement performed at 0.65 MPa.

- The light delivery part includes two types of lasers, whose beams were piped through the same optical fiber: a CW laser diode for the PTT (LD830-ME-2W, 830 nm, 2 W, Thorlabs, Germany), controlled in current and temperature (controller TEC,5A/225W, ITC4005, Thorlabs, Germany) and a pulsed laser for the PA (Brilliant EaZy, Nd:Yag, 1064 nm, 330 mJ, 5 ns, 10 Hz, Quantel, France). The pulsed laser was frequency doubled with a KTP crystal at 532 nm (Eksma Optics, Lithuania). Optical components (neutral densities, linear polarizers and half-wave plates) were placed on the pulsed laser path in order to control the energy delivered through the fiber. A combination of mirrors and lens enabled to align both CW and pulsed lasers and direct both beams through the fiber. An additional focusing lens was added at the exit of the fiber in order to lower the beams diameter to 4 mm after the water balloon. Pulsed laser energy and CW power were controlled right after the water balloon before each experiment. Typical values were 150-300 μJ for the pulsed laser and 100-300 mW for the CW. An additional red light pencil laser (632 nm) is also added for alignment.

Biomedical Optics EXPRESS

- A platform (Image Guided Therapy, France) comprising a small animal holder, a transducer holder mounted on fully programmable 3D scanning stages and a programmable ultrasound single channel amplifier. This system allows performing a fast raster scan (10 mm/s) during the FUS-BBB opening and possibly PTT. Hot water is conveyed to the animal bed *via* plastic tubes to keep the body temperature of the animal stable during the therapy. The temperature of the circulating water is stabilized (Corio CP-BC4, Circulating themostat, Julabo, Germany).

The different acoustic and optical emissions and data acquisition were controlled with a computer. Prior PA signal recording, a band pass filter was applied [0.04-3.5 MHz] to the signal and averaged over a certain number of measurements. In the present experiments, as the temperature rise during the therapy was usually fast (less than 30 s), the PA signal was averaged over only two data acquisitions, therefore the pulsed laser fluence was adapted in order to perform all the measurements with a sufficiently high signal-to-noise ratio. The fluence was simultaneously monitored and recorded with a photodiode (PDA10A2, Thorlabs, Germany), for normalization of the PA signal.

One of the difficulties that could be encountered was the resistance of the water balloon to high optical power during PTT combined with PA thermometry. A series of tests were specifically performed to measure a possible fluence or power attenuation through the water balloon during 15 min measurements. No specific damage was noticed on the water balloon, that could be used for the whole experiment campaign. Optical attenuation remained sufficiently low through latex to be able to perform both PTT and PA measurements.

The proposed FUS/PTT protocol includes three consecutive steps: i) systemic administration of efficient photoabsorbers (NPs or others); ii) injection of intravascular microbubbles followed by the application of FUS, by using the transducer in its active mode, with calibrated sonication parameters allowing BBB opening; iii) application of the PTT with PA temperature monitoring with a calibrated optical irradiation dose inducing tumor cell death. At the present stage, the FUS-induced BBB opening is a process well controlled in our setup and validated by SPECT imaging (results presented hereafter). Work is in progress to identify the best photoabsorber candidate and, despite of the large number of publications on preclinical PTT [23], a balance is still to be found between light thermal dose that induces tumor cell death and minimum damages caused to healthy surrounding tissues. The present setup is developed to that purpose.

2.2. Photothermal therapy and temperature monitoring with photoacoustics

The purpose of thermal therapy consists in generating target temperatures typically of 48-50°C (they can go up to 95-100°C in some studies). Tissue cells destruction is often defined by the 50-54°C boundary and a lethal thermal dose exposure of t_{43}>240 − 540 min in human beings [43], where t_{43} is the time that one should have spent at 43°C, temperature chosen as a reference, to reach the same biological effect, also called thermal dose [44]: $t_{43} = \int_{initial}^{final} R^{43-T} dt$, where T is the temperature and R is a parameter equal to 0.25 below 43°C and 0.5 above. The duration of thermal exposure varies, depending upon the type of heating modality, target location and dimensions, temperature distributions and treatment strategy. The laser parameters selected for this *in vivo* study (laser wavelength, power and heating duration) were based on values taken from literature [23] and the efficacy results obtained *in vitro* on U87-MG spheroids using TiN NP [24]. The local dose of TiN NP administered intratumorally in the present studies corresponded to the highest safe dose obtained in the *in vitro* studies without laser exposure, to avoid local toxicities induced by the nanoparticles. Our objective was to irradiate the tumor and achieve a slow hyperthermic exposure lasting more than 2 min at temperatures in the range of 44-55°C, to obtain a temperature homogeneity throughout the exposure site and efficiently kill all tumor cells [23,45].

The photoacoustic pressure wave is proportional to both the locally deposited optical fluence $A(\mathbf{r}, \mu_a(\mathbf{r}), \mu_s'(\mathbf{r}))$, where $\mu_a(\mathbf{r})$ and $\mu_s'(\mathbf{r})$ are the absorption and the reduced scattering coefficients,

Biomedical Optics EXPRESS

and the Grueseinen coefficient $\Gamma(\mathbf{r}) = \beta(\mathbf{r})c^2(\mathbf{r})/C_p(\mathbf{r})$, that accounts for the mechanical properties of the medium, the volume expansion coefficient β, the speed of sound c and the heat capacity at constant pressure C_p.

For water-based and fatty tissues, the volume expansion coefficient and the speed of sound are both temperature dependent and, between 10 and 55 °C, linearly proportional to the temperature [46,47]. Therefore, the Grueneisen parameter, and thus the photoacoustic signal, can be directly related to temperature. Within the linear approximation, it can be approximated as $\Gamma = A + BT$, where A and B are constant parameters depending on the mechanical properties of the tissue, and T is the temperature [48]. Hence, as long as the dependence between temperature and Γ can be supposed to be linear, one can link the variation of the amplitude of the PA pressure ΔP directly to the temperature rise ΔT [27,28,36]:

$$\frac{\Delta P}{P_o} = \alpha \frac{\Delta \Gamma}{\Gamma_o} = \alpha \Delta T, \tag{1}$$

where P_o is the amplitude of the PA signal at a reference temperature T_o and α is a calibration factor to be evaluated for the probed sample. The adopted calibration protocol is described in section 3.2.

2.3. *In vivo protocols*

All *in vivo* experiments reported in this work were approved by the institutions Animal Care and Use Committee (CE71, Aix-Marseille Université) and performed following the French national regulation guidelines in accordance with EU Directive 2010/63/EU. The animals used for this work were six-week-old female athymic Nude-Foxn1nu mice (Envigo, France). Animals were housed in enriched cages placed in a temperature- and hygrometry-controlled room with daily monitoring and had free access to water and food.

2.3.1. Blood-brain barrier permeabilization induced by focused ultrasound sonication

Local, transient and safe disruption of the BBB can be achieved by using low power pulsed FUS combined with intravascular microbubbles [41,49]. Because it allows the delivery to the CNS of large molecules, FUS-induced BBB permeabilization has opened new avenues in chemotherapies such as anticancer drugs [50], anti-amyloid antibodies [51], anti-cancer antibodies [52] or nanoparticles [53] that are unable to cross the BBB. The optimal parameters for BBB disruption such as the influence of ultrasound parameters, microbubble properties, or the physiologic state of the animals (temperature, anesthesia) are starting to be well controlled and physical mechanisms better understood [41,49,54]. In this work, the BBB disruption parameters were adapted from previously reported studies based on the characteristics of our transducer and the opening was verified by SPECT.

For the BBB permeabilization studies, one healthy animal was anesthetized by intraperitoneal injection of ketamine/xylazine (100 and 10 mg/kg, respectively) and placed in dedicated temperature-controlled frame in prone position under the setup. One hundred microliters of Sonovue microbubbles (Bracco, Italy) were systemically administered *via* retro-orbital injection in the right eye using an insulin syringe (27 G) and a single spot sonication sequence was applied (1.5 MHz frequency, pulse length of 3 ms every 100 ms for 2 min with *in situ* peak negative pressure of 0.52 MPa calibrated in free water [55].

2.3.2. Single photon emission computed tomography imaging

The BBB opening was confirmed by SPECT imaging using pentetic acid (DTPA) as radiotracer. Following sonication, ^{99m}Tc-DTPA was administered using an insulin syringe (27 G) by intravenous injection of 50 μl of radioactive tracer (20 MBq) in isotonic and pyrogen-free solution; 30 minutes after injection, the SPECT-CT acquisition was applied for 20 minutes under

Biomedical Optics EXPRESS

anesthesia with 1.5% vol isoflurane (IsoVet, Vetosante) using a NanoSPECT/CT Plus camera (Mediso Medical Imaging System Ltd) and the Nucline 1.02 software (Mediso Medical Imaging System Ltd). CT parameters were X-ray, 45 kVp, exposition 500 ms, binning 1:4, and projection 180. Aperture was pinhole 102 Rat STD, whole body 2.2 mm. SPECT and CT dicom files were fused for reconstruction and image treatment using Invicro VivoQuant 3.5 and Invicro InvivoScope 2.00 reconstruction softwares (Boston, USA) to assess the tracer uptake in the brain.

2.3.3. Photothermal therapy and temperature monitoring with photoacoustics

U87-MG glioma cells (ATTC, USA) were cultured in Eagle's Minimum Essential Medium (EMEM; Gibco, Life Technologies, USA). The medium was supplemented with 10% Fetal Bovine Serum (FBS; Gibco, Life Technologies USA), 100 U/mL penicillin G sodium and 100 μg/mL streptomycin sulfate (Gibco, Life Technologies, USA). Cells were subcultured in 75 cm^2 culture flasks (Corning T-75, Sigma-Aldrich, USA) and incubated at 37°C and 5% CO_2.

For the subcutaneous *in vivo* studies, animals were anesthetized by intraperitoneal injection of ketamine/xylazine (100 and 10 mg/kg, respectively) and U87-MG cells were injected subcutaneously between the shoulders (2×10^6 cells/mouse). Tumor size was measured every other day using an electronic caliper and the volumes were calculated using the formula corresponding to a prolate ellipsoid: volume = $\pi/6 \times$ length $\times$ width^2. When the tumors reached the volume of about 20 mm^3 (approximately two weeks after cells injection), mice were randomized into 3 groups and treated as follows: Group 1: calibration group, TiN NP intratumoral injection (30 μl, 4 mg/ml), one thermocouple was inserted surgically inside the tumor, followed by laser irradiation (n=3); Group 2: laser irradiation (n=3); Group 3: TiN NP intratumoral injection (30 μl, 4 mg/ml) followed by laser irradiation (n=3). TiN NP (GetNanoMaterials, France) were dispersed in MilliQ water (4 mg/ml), mixed under magnetic stirring (300 rpm) and sonicated by ultrasonic probe for 5 minutes. The average size was measured following dilution in water (ratio 1:400) by dynamic light scattering using a Zetasizer Nano ZS apparatus (Malvern) and was 165 ± 3 nm, (n=3, mean ± standard deviation). The day of treatment, animals were anesthetized by intraperitoneal injection of ketamine/xylazine (100 and 10 mg/kg, respectively) and 300 μl of physiological solution pre-heated at 37°C were administered subcutaneously in their flank to avoid anesthetic-induced hypothermia and dehydration prior to treatment administration. Then, they were placed in dedicated temperature-controlled frame in prone position under the setup and the TiN NP were intratumorally injected (groups 1 and 3). The tumors were irradiated for 4 to 12 min by the CW NIR laser diode (4.5 W.cm^{-2}) for PTT and by the pulsed laser (2.1 mJ.cm^{-2}) for PA measurement. After the treatment and temperature monitoring protocol, the animals were sacrificed by cervical dislocation.

For the proof-of-concept transcranial study on orthotopic model, animals were anesthetized by intraperitoneal injection of ketamine/xylazine (100 and 10 mg/kg, respectively), and fixed in a stereotactic frame. The skin surface on the head was disinfected by application of an antiseptic solution (Vétédine solution, France), lidocaine (10 mg/ml) was injected subcutaneously at the sites of incision, the eyes were protected with an ophthalmic gel (Ocry-gel, France) and 200 μL of physiological solution were injected subcutaneously in the flank to hydrate the animal. A 5 mm long incision was made along the midline and a burr hole was drilled into the skull at the right frontal lobe, 0.5 mm anterior and 2 mm lateral to the bregma (high speed drill: Tack life, USA; 0.8 mm diameter round end engraving burrs: Dremel, USA). A 10 μL 26 G syringe with cemented 51 mm needle (Hamilton, USA) was used to inject 5×10^4 U87-MG cells suspended in EMEM (without FBS and antibiotics) at a depth of 3.0 mm from the outer border of the brain, using an automatic pump device at a speed of 0.7 μl/min. The wound was then closed using a tissue adhesive glue (3M Vetbond, France) and the animals recovered under an infrared heating lamp. Eleven days later, the animals were anesthetized, fixed on the stereotactic frame and the surface opened again as previously mentioned. On one animal, 10 μl of TiN NP (4

Biomedical Optics EXPRESS

mg/ml) were injected in the previous burr hole at the same coordinates using an Hamilton syringe. Another animal was left untreated. For both animals, the stereotactic frame was placed under the integrated setup for PTT and PA monitoring directly on contact with the skull. In order to prevent brain damages, the light irradiation dose was limited to ~ 1 W.cm $^{-2}$ for this experiment, the energy of the pulsed laser was kept unchanged. In order to probe a sub-skull area, the water balloon was inflated to 7 mm, corresponding to a 3 mm depth from the surface of the head of the animal.

3. Results

In this section is presented an experimental validation of the BBB permeabilization and are described the calibration protocol and two preliminary illustrative experiments of PTT and PA thermometry: one is performed on mice bearing subcutaneous tumors, the second is a transcranial experiment.

3.1. Blood-brain barrier permeabilization and single photon emission computed tomography imaging

Figure 3 shows an example of a single spot opening in a healthy mouse performed using the fully integrated device. The animal was imaged by SPECT-CT 30 minutes following sonication.

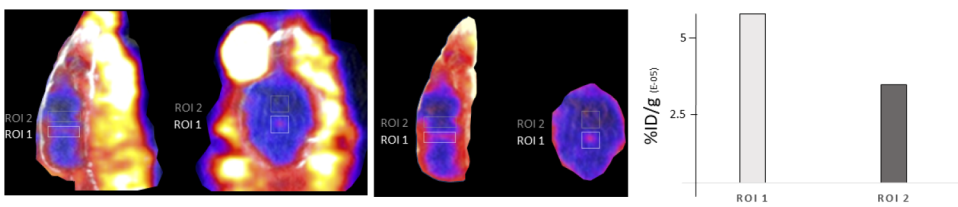

Fig. 3. Example of BBB disruption 30 minutes after single-spot focused ultrasound and ^{99m}Tc-DTPA intravenous injection in a healthy mouse. *Left*: representative SPECT tomographic image of ^{99m}Tc-DTPA distribution in the head of the animal merged with CT (the contours of the skull are visible in white) with sagittal (left) and coronal (right) sections. Two regions of interest (ROI) are highlighted with white rectangles: ROI 1 is the sonicated volume, ROI 2 is an untreated zone. *Center*: Segmentation in the brain area. *Right*: Quantification of ^{99m}Tc-DTPA activity in ROI 1 and ROI 2. Results are expressed as percentage of injected activity per mass of tissue (%ID/g).

Results are expressed as percentage of injected dose per mass of tissue (%ID/g). Figure 3 shows a high level of activity everywhere in the head of the animal except in the brain and at the sonication spot (ROI 1). As the DTPA tracer does not cross the BBB except at the sonication spot, this confirms the local BBB permeabilization. The concentration map and quantifications show that the amount of ^{99m}Tc-DTPA is higher in the sonicated area (center of the brain), that penetrates the whole brain in depth (sagittal view), than in the rest of the brain 30 min after sonication and injection of the radiotracer, confirming that the device is functional for this purpose. No side effects nor sign of pain or distress was observed in the animals following this sonication protocol. This experiment confirms that the integrated device is fully operational for the BBB opening application.

3.2. Photothermal therapy and temperature monitoring with photoacoustics: calibration measurements on subcutaneous gbm model (group 1)

The water balloon was inflated in order to position the tranducer focal point subcutaneously, inside the tumor of GBM-grafted mice. Degassed acoustic gel was used to couple the transducer

Biomedical Optics EXPRESS

membrane to the skin. Temperature calibration was performed by using a digital thermometer with two pre-calibrated thermocouples (RS Pro APPA 55II, RS Components, France), one placed at the top surface of the skin of the animal, the other inserted surgically to monitor the intratumoral temperature (Fig. 4, Left).

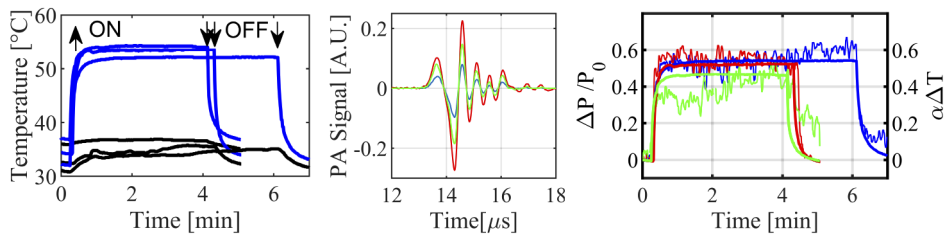

Fig. 4. *Left*: Surface (black curves) and intratumoral (blue curves) temperature measurements with thermocouples for three animals for PTT times of 4, 5 and 6 minutes (upward arrow, CW illumination 'ON': beginning of the PTT; downward arrow, CW illumination 'OFF': end of the PTT); *Center*: Example of time-resolved PA measurement, during a 5 minutes PTT, at three different heating times 0.006 min (rising slope, in blue), 2.3 min (plateau, in red) and 5 min (downward slope); *Right*: Calculated values of ratios $\Delta P/P_o$ (thin lines) and $\alpha\Delta T$ (thick lines), $\alpha = 0.027 \pm 0.003$ °C^{-1}.

PTT was applied for a period of 4 to 6 minutes in these preliminary tests. The CW laser power was 520 mW (~ 7 W.cm^{-2}) and PA energy 150 μJ (~ 2 mJ.cm^{-2}), both controlled at the exit of the water balloon. Regarding the thermocouples temperature measurements, a classical response to an ON/OFF heating cycle was measured: the heating profile follows a steep increase in the first minute before reaching a plateau (saturation) when heat dissipation equilibrium is reached. It was observed a limited increase at the skin surface (see black curves in Fig. 4, Left), between 1.8°C and 4.3°C, while a much higher temperature is reached within the tumor, as an increased comprised between 17.5°C and 20.2°C was measured (same figure, blue curves, reaching temperatures between 50°C and 55°C.

The simultaneously measured PA signals were measured with a maximum amplitude at 14.3 μs. Considering the speed of sound close to the one of water (1500 m.s^{-1}), the corresponding probed depth was 2.15 cm, close to the focal position at 2 cm, collocated here with the skin surface. The entire measured signal corresponded to a subsurface region, containing the tumor. As the focal volume probed by the transducer corresponds to approximately a 6 mm depth, one can consider the PA signal is resulting from the collective response of the sample heated within the whole focal volume. Here, we made the assumption that the PA monitored temperature corresponded to the intratumoral temperatures (blue curves in Fig. 4, Left). The recorded PA time-resolved signals were first normalized to the maximum of amplitude of the pulsed laser measured simultaneously. A median filter (order 10) was applied. Peak-to-peak amplitudes were obtained from these curves (Fig. 4, Center). Increase and decrease of the PA amplitudes were found to correlate well with the temperature values. The FUS transducer was designed to maximize the energy transmission in the forward direction, for efficient BBB opening. It was manufactured using a high power bowl-shaped single element piezoelectric with no backing layer. The absence of this damping layer affects the measured signal showing these so-called "ringing effect" oscillations [56]. In Fig. 4, Right, are plotted the ratios $\Delta P/P_o$ and $\alpha\Delta T$ (Eq. (1)) for the 3 mice. From these measurements, the calibration factor was found: $\alpha = 0.027 \pm 0.003$°C^{-1} as the value minimizing $\|\frac{\Delta P}{P_o} - \alpha\Delta T\|$. Prior calculating $\Delta P/P_o$, the PA signals were shifted to correct for the changes of the speed-of-sound due to the increase of temperature.

Biomedical Optics EXPRESS

3.3. Photothermal therapy and temperature monitoring with photoacoustics: preliminary tests on subcutaneous GBM model (Groups 2 and 3)

The water balloon was inflated to 10 mm for this experiment to collocate the position of the center of the focal volume with the skin surface of the animal (no compression). The duration of the CW light irradiation was 10 min. The PA registered signals are presented in Fig. 5, for Groups 2 and 3. In all the measurements, the signals were acquired during a time interval corresponding to the ultrasound propagation time from the focus to the transducer, between 13.5 and 19 μs. To ease the interpretation, the time-resolved PA signals are plotted as a function of the estimated distance from the center of the focal spot, supposed to be at 2 cm from the transducer surface.

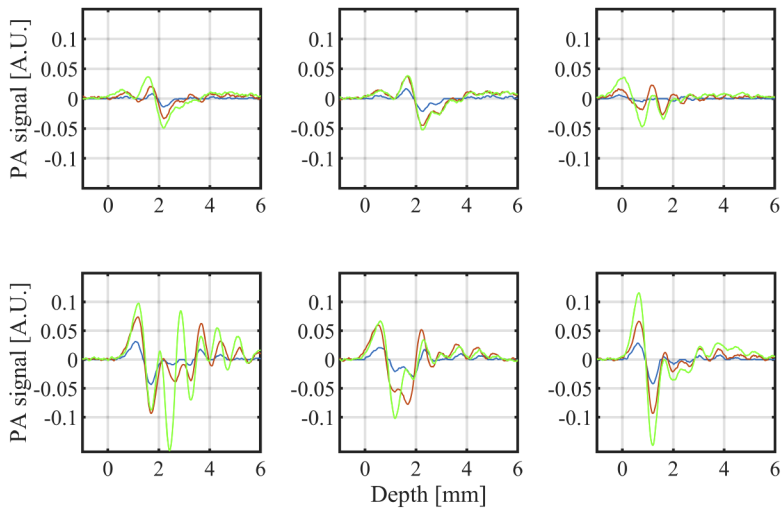

Fig. 5. *Top*: PA registered signals [A.U.] during a 10 min PTT for the three mice of Group 2 (without NPs), for 0.007 min (blue), 1 min (red) and 8.5 min (green)

The temperature variations during PTT (ΔT), estimated by considering the previously determined calibration factor, for Group 2 (left) and Group 3 (right) are plotted in Fig. 6.

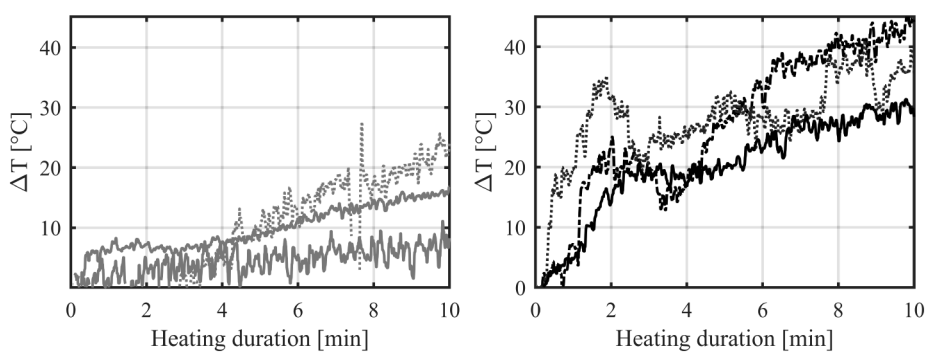

Fig. 6. Evolution of the estimated temperature rise during the PTT on Group 2 (*Left*) and Group 3 (*Right*) mice.

Biomedical Optics EXPRESS

3.4. Photothermal therapy and temperature monitoring with photoacoustics: transcranial proof-of-concept experiment on orthotopic GBM model

A feasibility test of transcranial PTT was performed on two mice grafted with an orthotopic tumor grafted. One mouse was intratumorally injected with TiN NP, and the other was left untreated but both were submitted to irradiation on top of the scalp. The water balloon was inflated to 9 mm for this experiment and pushed 2 mm on top of the skull to collocate the position of the center of the focal volume with the location of the tumor cells within the brain. The duration of the CW light irradiation was 10 min. The results are presented on Fig. 7.

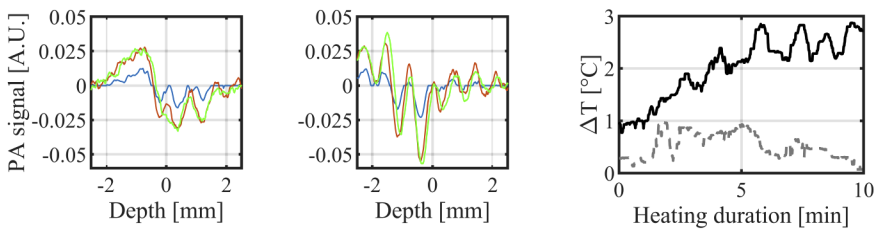

Fig. 7. PA registered signals [A.U.] during a 10 min PTT for a mouse without NPs (*left*) and a mouse with NPs (*middle*) at 0.007 min (blue), 1 min (red) and 8.5 min (green). For a better readability, only one signal per minute is represented. *Right*: Estimated temperature rise during the PTT for the mouse with (Black curve) and without (Grey curve) NPs.

4. Discussion

The preliminary tests on subcutaneous GBM model show the effect of using NPs (Fig. 5). For Group 2, the PA signal is weak. The use of TiN NPs clearly produces a strong enhancement of the amplitudes of the signal measured on mice from Group 3 that received TiN-NP intratumoral injection. In all these measurements, a front N-shaped signal (Fig. 5, Bottom) was observed, followed by oscillations that are not only due to "ringing effects". Amplitudes of these signals vary for each situation, depending on the physiology of the animal (color and thickness of the skin, vascularization and density of the tumor, site of injection of the NPs in the present case, for example), the amplitude of the first signal can be higher or lower than the following ones. Despite the high volume of data, recording the whole PA signals is therefore very instructive as sensitive to the tissue composition in depth and to the local mechanical variations. In all cases, the curves were corrected by the time-shift due to the variations of the speed of sound as a function of the temperature increase. However, this dependence of the speed of sound on temperature is relatively weak ($\sim$1 m.s^{-1}.°C^{-1}) but highly depending on the nature of the tissues [46,47], increasing with temperature in muscle, and other tissues with high water content, but decreasing in fatty tissues [57], as it was the case here. This can provide some indications on the nature of the probed surface and tumorous tissues. In the present experiment, most of the time, a right-shift of the PA signal was observed, indicating a high fat content in the probed tissues. Coagulation and dehydration cause modifications in the structure of the tissue that also lead to changes in the speed of sound. However, the change in the speed of sound is very limited (a few percent) for all kinds of soft tissues in the temperature range of 30°C to 80°C. The control and the efficacy of the therapy will depend on all these factors (tissue composition and evolution of the tissue structure during PTT). This illustrates the importance of monitoring the amplitude of signal and how it is affected by heating in depth.

Without NPs (Group 2), the temperature rise remains weak in the first five minutes (8°C maximum) while a slow linear increase is observed after, showing the difficulty in performing PTT without absorption contrast agents. In a same time, this demonstrates the limited thermal

Biomedical Optics EXPRESS

side-effect expected if the targeting of the NPs were efficient. With NPs (Group 3), in the two first minutes of heating, all the curves approximately follow the same trend. In the first minute, they slowly increase, before following a steepest increase slope. This delay can be due to the effect of perfusion in the vascular system. After 2 min, the slope changes and, depending on the animal, it can reach a plateau or decrease. This change in the slope has been reported and is a hint of the coagulation process. Nikitin *et al.* [29], using a point illumination laboratory setup as can be considered the case in the present situation (beam with small diameter), have reported these behaviors for excised porcine tissues: decreasing for fatty tissue (lard) and increasing for a highly vascularized organ (liver). Similarly here, these measurements indicate tissues with a mixture of fat and vascularized tissues. Indeed, tumor cells were grafted subcutaneously in the back, between the shoulders, therefore tumors developed between the supraspinal and suprascapular region. These regions contain fat depots composed of white and brown adipose tissues, with different colors, consistences and thermogenic activities [58] which might behave differently to the laser exposure but also lead to different tumor cell metabolism following treatment in terms of glucose and fatty acids consumption. Moreover, the adipose amount, tumor location and skin thickness can vary between animals leading to heterogeneous PTT responses. After 4 min, the slope can eventually increase, leading to temperatures variations as high as 30°C to 40°C after 10 min exposure, indicating the coagulation due to the high blood content of the organ.

The feasibility of using the device for transcranial measurements is illustrated (Fig. 7). A broad skull response was measured first, present without and with NPs, after which higher perturbations were observed when NPs were injected. Here again, the amplitude of the PA signal with NPs exhibits higher amplitude and additional features. However, the estimated temperature rise (Fig. 7, left) appears insufficient (maximum 2.5°C) with the low dose light irradiation used and the heating process would take advantage of a multi-spot illumination. Nevertheless, this experiment shows the feasibility in performing transcranial PTT combined with PA monitoring with this setup and illustrates its versatility and ergonomy.

After analyzing these preliminary results, several avenues for improvements appear. First, the setup might be improved in order to achieve PA imaging functionalities. Indeed, in order to offer a compact theranostic solution, the priority was on energy transmission for BBB opening and no backing material was used. As a consequence, the use of the same transducer for measurements offers a reasonably high sensitivity and efficiency but also suffers from undesirable long narrow bandwidth oscillations that limit imaging performances. For this purpose, a dedicated multi-zone annular transducer might be designed in the future. The central imaging part should have a backing layer to increase its bandwidth and the outer therapeutic annulus would be an air-backing transducer to maximize energy transmission.

Additionally, a more sophisticated PA calibration resolved in depth could also be performed, through the measurement of the instrument response function, deconvolution of the PA signals and back-propagating them along the transducer axis [59].

Uncoupling effects due to temperature on the mechanical properties from those on the tissue composition is challenging. This should be achieved by multiple wavelength measurements that would enable to follow the changes in the composition of the tissues during the therapy and to predict the resulting effect of the temperature on the mechanical properties.

Finally, a more integrated setup can also be obtained by using new pulsed laser diodes as PA source [32].

5. Conclusion

An original multipurpose integrated setup has been developed for efficient PTT of the glioblastoma in small animals. It allows combining for the first time i) BBB opening by FUS for an increased efficiency in the targeted drug delivery to the brain; ii) PTT and iii) *in situ* temperature monitoring with PA. The FUS-induced BBB opening step is well controlled, confirmed here

Biomedical Optics EXPRESS

by SPECT imaging. Sub-cutaneous and transcranial preliminary experiments were performed and demonstrated that the whole device is functional. PTT with PA temperature monitoring was tested and the preliminary measurements show the complexity of the PTT and revealed opto-acousto-thermal coupled effects within the tissue structures. Therefore, using the PA as thermometer is not straightforward and quite challenging, but brings some complementary information on the course of the treatment, or on the efficacy of the photoabsorbers used. Potentially, it can offer real time quantification and can lead to a personalized medicine taking into account the composition of the probed tissues.

The flexibility of the setup allows an easy adaptation for hybrid thermal treatments [60], combining PTT and FUS, by favorably using the same transducer for BBB opening, thermal heating and PA. Such hybrid treatment may result in synergetic effects of both modalities.

Non-invasive transcranial PTT has been shown feasible. The optimisation of the thermal dose remains challenging, the present setup paves the way for appropriate treatment with real-time temperature monitoring. An optimized device, based on the improvement of this first prototype, should be able to perform the whole theranostic protocol through skull in GBM mice models, i.e. photoabsorber delivery to the tumor after BBB disruption followed by PTT monitored by PA.

Funding. ITMO "Plan Cancer 2014–2019" INSERM program (PC201613).

Acknowledgments. The authors are grateful to Nicola Jones for her contribution to the numerical control of the FUS system. This project is developed in the field of the "Glioblastoma Risk Attrition by Vectorized Thermotherapy - GRAVITY" project (PC201613) funded by the ITMO "Plan Cancer 2014–2019" INSERM program.

Disclosures. The authors declare that there are no conflicts of interest related to this article.

References

1. J. N. Sarkaria, G. J. Kitange, C. D. James, R. Plummer, H. Calvert, M. Weller, and W. Wick, "Mechanisms of chemoresistance to alkylating agents in malignant glioma," Clin. Cancer Res. **14**(10), 2900–2908 (2008).
2. S. A. Grossman and J. F. Batara, "Current management of glioblastoma multiforme," Semin. Oncol. **31**(5), 635–644 (2004).
3. E. Alphandéry, "Nano-therapies for glioblastoma treatment," Cancers **12**(1), 242 (2020).
4. C. Ferraris, R. Cavalli, P. Panciani, and L. Battaglia, "Overcoming the blood-brain barrier: successes and challenges in developing nanoparticle-mediated drug delivery systems for the treatment of brain tumours," Int. J. Nanomed. **15**, 2999–3022 (2020).
5. C. Bastiancich, P. Danhier, V. Preat, and F. Danhier, "Anticancer drug-loaded hydrogels as drug delivery systems for the local treatment of glioblastoma," J. Controlled Release **243**, 29–42 (2016).
6. A. Dasgupta, M. Liu, T. Ojha, G. Storm, F. Kiessling, and T. Lammers, "Ultrasound-mediated drug delivery to the brain: principles, progress and prospects," Drug Discovery Today: Technol. **20**, 41–48 (2016).
7. K. Hynynen, N. McDannold, N. Vykhodtseva, and F. Jolesz, "Noninvasive MR imaging-guided focal opening of the blood-brain barrier in rabbits," Radiology **220**(3), 640–646 (2001).
8. T. Mainprize, N. Lipsman, Y. Huang, Y. Meng, A. Bethune, S. Ironside, C. Heyn, R. Alkins, M. Trudeau, A. Sahgal, J. Perry, and K. Hynynen, "Blood-brain barrier opening in primary brain tumors with non-invasive MR-guided focused ultrasound: a clinical safety and feasibility study," Sci. Rep. **9**(1), 321 (2019).
9. E. S. Glazer and S. A. Curley, "The ongoing history of thermal therapy for cancer," Surg. Oncol. Clin. N. Am. **20**(2), 229–235 (2011).
10. I. Mellal, A. Oukaira, E. Kengene, and A. Lakhssassi, "Thermal therapy modalities for cancer treatment: a review and future perspectives," Appl. Sci. Res. Rev. **04**(02), 1–11 (2017).
11. R. Riley and E. Day, "Gold nanoparticle-mediated photothermal therapy: applications and opportunities for multimodal cancer treatment," Wiley Interdiscip Rev. Nanomed Nanobiotechnol. **9**(4), e1449 (2017).
12. G. Baffou and R. Quidant, "Thermo-plasmonics: using metallic nanostructures as nano-sources of heat," Laser Photonics Rev. **7**(2), 171–187 (2013).
13. Y.-C. Tsai, P. Vijayaraghavan, W.-H. Chiang, H.-H. Chen, T.-I. Liu, M.-Y. Shen, A. Omoto, M. Kamimura, K. Soga, and H.-C. Chiu, "Targeted delivery of functionalized upconversion nanoparticles for externally triggered photothermal/photodynamic therapies of brain glioblastoma," Theranostics **8**(5), 1435–1448 (2018).
14. W. Lu, M. P. Melancon, C. Xiong, Q. Huang, A. Elliott, S. Song, R. Zhang, L. G. Flores, I. I. J. G. Gelovani, L. V. Wang, G. Ku, R. J. Stafford, and C. Li, "Effects of photoacoustic imaging and photothermal ablation therapy mediated by targeted hollow gold nanospheres in an orthotopic mouse xenograft model of glioma," Cancer Res. **71**(19), 6116–6121 (2011).
15. L. Ricciardi, L. Sancey, G. Palermo, R. Termine, A. De Luca, E. I. Szerb, I. Aiello, M. Ghedini, G. Strangi, and M. La Deda, "Plasmon-mediated cancer phototherapy: the combined effect of thermal and photodynamic processes," Nanoscale **9**(48), 19279–19289 (2017).

Biomedical Optics EXPRESS

16. J. Chen, Z. Sheng, P. Li, M. Wu, N. Zhang, X.-F. Yu, Y. Wang, D. Hu, H. Zheng, and G. P. Wang, "Indocyanine green-loaded gold nanostars for sensitive SERS imaging and subcellular monitoring of photothermal therapy," Nanoscale **9**(33), 11888–11901 (2017).
17. D. P. N. Goncalves, R. D. Rodriguez, T. Kurth, L. J. Bray, M. Binner, C. Jungnickel, F. N. Guer, S. W. Poser, T. L. Schmidt, D. R. T. Zahn, A. Androutsellis-Theotokis, M. Schlierf, and C. Werner, "Enhanced targeting of invasive glioblastoma cells by peptide-functionalized gold nanorods in hydrogel-based 3D cultures," Acta Biomater. **58**, 12–25 (2017).
18. Z. Wang, P. Huang, O. Jacobson, Z. Wang, Y. Liu, L. Lin, J. Lin, N. Lu, H. Zhang, R. Tian, G. Niu, G. Liu, and X. Chen, "Biomineralization-inspired synthesis of copper sulfide-ferritin nanocages as cancer theranostics," ACS Nano **10**(3), 3453–3460 (2016).
19. J. T. Robinson, S. M. Tabakman, Y. Liang, H. Wang, H. S. Casalongue, D. Vinh, and H. Dai, "Ultrasmall reduced graphene oxide with high near-infrared absorbance for photothermal therapy," J. Am. Chem. Soc. **133**(17), 6825–6831 (2011).
20. M. Qian, Y. Du, S. Wang, C. Li, H. Jiang, W. Shi, J. Chen, Y. Wang, E. Wagner, and R. Huang, "Highly crystalline multicolor carbon nanodots for dual-modal imaging-guided photothermal therapy of glioma," ACS Appl. Mater. Interfaces **10**(4), 4031–4040 (2018).
21. O. Akhavan and E. Ghaderi, "Graphene nanomesh promises extremely efficient in vivo photothermal therapy," Small **9**(21), 3593–3601 (2013).
22. B. Guo, Z. Sheng, D. Hu, A. Li, S. Xu, P. N. Manghnani, C. Liu, L. Guo, H. Zheng, and B. Liu, "Molecular engineering of conjugated polymers for biocompatible organic nanoparticles with highly efficient photoacoustic and photothermal performance in cancer theranostics," ACS Nano **11**(10), 10124–10134 (2017).
23. C. Bastiancich, A. Da Silva, and M.-A. Estève, "Photothermal therapy for the treatment of glioblastoma: potential and preclinical challenges," Front. Oncol. **10**, 610356 (2021).
24. A. A. Popov, G. Tselikov, N. Dumas, C. Berard, K. Metwally, N. Jones, A. Al-Kattan, B. Larrat, D. Braguer, S. Mensah, A. Da Silva, M.-A. Estève, and A. V. Kabashin, "Laser-synthesized TiN nanoparticles as promising plasmonic alternative for biomedical applications," Sci. Rep. **9**(1), 1194 (2019).
25. W. He, K. Ai, C. Jiang, Y. Li, X. Song, and L. Lu, "Plasmonic titanium nitride nanoparticles for in vivo photoacoustic tomography imaging and photothermal cancer therapy," Biomaterials **132**, 37–47 (2017).
26. I. Larina, K. Larin, and R. Esenaliev, "Real-time optoacoustic monitoring of temperature in tissues," J. Phys. D: Appl. Phys. **38**(15), 2633–2639 (2005).
27. J. Shah, S. Park, S. Aglyamov, T. Larson, L. Ma, K. Sokolov, K. Johnston, T. Milner, and S. Y. Emelianov, "Photoacoustic imaging and temperature measurement for photothermal cancer therapy," J. Biomed. Opt. **13**(3), 034024 (2008).
28. S.-H. Wang, C.-W. Wei, S.-H. Jee, and P.-C. Li, "Photoacoustic temperature measurements for monitoring of thermal therapy," in *Photons Plus Ultrasound: Imaging And Sensing 2009*, vol. 7177 *of Proceedings of SPIE* A. A. Oraevsky and L. V. Wang, eds., (SPIE; Fairway Med Technol, Inc, 2009). Conference on Photons Plus Ultrasound - Imaging and Sensing 2009, San Jose, CA, JAN 25-28, 2009.
29. S. M. Nikitin, T. D. Khokhlova, and I. M. Pelivanov, "Temperature dependence of the optoacoustic transformation efficiency in ex vivo tissues for application in monitoring thermal therapies," J. Biomed. Opt. **17**(6), 061214 (2012).
30. Y.-S. Hsiao, X. Wang, and C. X. Deng, "Dual-wavelength photoacoustic technique for monitoring tissue status during thermal treatments," J. Biomed. Opt. **18**(6), 067003 (2013).
31. X. Jian, N. Wang, C. Yang, Z. Han, J. Xu, Z. Li, Y. Cui, and F. Dong, "Multiwavelength photoacoustic temperature measurement with phantom and ex-vivo tissue," Opt. Commun. **457**, 124724 (2020).
32. P. K. Upputuri, D. Das, M. Maheshwari, Y. Yaowen, and M. Pramanik, "Real-time monitoring of temperature using a pulsed laser-diode-based photoacoustic system," Opt. Lett. **45**(3), 718–721 (2020).
33. K. Daoudi, P. van Es, S. Manohar, and W. Steenbergen, "Two-dimensional spatiotemporal monitoring of temperature in photothermal therapy using hybrid photoacoustic-ultrasound transmission tomography," J. Biomed. Opt. **18**(11), 116009 (2013).
34. F. J. O. Landa, X. L. Dean-Ben, R. Sroka, and D. Razansky, "Volumetric optoacoustic temperature mapping in photothermal therapy," Sci. Rep. **7**(1), 9695 (2017).
35. E. Petrova, S. Ermilov, R. Su, V. Nadvoretskiy, A. Conjusteau, and A. Oraevsky, "Using optoacoustic imaging for measuring the temperature dependence of Gruneisen parameter in optically absorbing solutions," Opt. Express **21**(21), 25077–25090 (2013).
36. L. W. H. Ke and S. Tai, "Photoacoustic thermography of tissue," J. Biomed. Opt. **19**(2), 026003 (2014).
37. J. Yao, H. Ke, S. Tai, Y. Zhou, and L. V. Wang, "Absolute photoacoustic thermometry in deep tissue," Opt. Lett. **38**(24), 5228–5231 (2013).
38. V. P. Nguyen, J. Kim, K.-l. Ha, J. Oh, and H. W. Kang, "Feasibility study on photoacoustic guidance for high-intensity focused ultrasound-induced hemostasis," J. Biomed. Opt. **19**(10), 105010 (2014).
39. X. Wu, J. L. Sanders, D. N. Stephens, and O. Oralkan, "Photoacoustic-imaging-based temperature monitoring for high-intensity focused ultrasound therapy," in *2016 38th Annual International Conference Of The IEEE Engineering in Medicine and Biology Society (EMBC)*, (IEEE Engn Med & Biol Soc, 2016), pp. 3235–3238.

Biomedical Optics EXPRESS

40. J. Kim, W. Choi, E.-Y. Park, Y. Kang, K. J. Lee, H. H. Kim, W. J. Kim, and C. Kim, "Real-time photoacoustic thermometry combined with clinical ultrasound imaging and high-intensity focused ultrasound," IEEE Trans. Biomed. Eng. **66**(12), 3330–3338 (2019).
41. R. Magnin, F. Rabusseau, F. Salabartan, S. Meriaux, J.-F. Aubry, D. Le Bihan, E. Dumont, and B. Larrat, "Magnetic resonance-guided motorized transcranial ultrasound system for blood-brain barrier permeabilization along arbitrary trajectories in rodents," J. Ther. Ultrasound **3**(1), 22 (2015).
42. H. Assi, C. Yang, E. Shaswary, M. Tam, J. Tavakkoli, M. Kolios, G. Peyman, and C. Kumaradas, "Real-time control of nanoparticle-mediated thermal therapy using photoacoustic imaging," IEEE Transactions on Biomedical Engineering, pp. 1, 10.1109/TBME.2020.3037991 (2020).
43. C. J. Diederich, "Thermal ablation and high-temperature thermal therapy: Overview of technology and clinical implementation," Int. J. Hyperthermia **21**(8), 745–753 (2005).
44. S. Sapareto and W. Dewey, "Thermal Dose Determination in Cancer-Therapy," Int. J. Radiat. Oncol., Biol., Phys. **10**(6), 787–800 (1984).
45. P. X. E. Mouratidis, I. Rivens, J. Civale, R. Symonds-Tayler, and G. ter Haar, "Relationship between thermal dose and cell death for "rapid" ablative and "slow" hyperthermic heating," Int. J. Hyperthermia **36**(1), 228–242 (2019).
46. F. A. Duck, *Physical Properties of Tissues* (Academic Press, 1990).
47. J. Bamber and C. Hill, "Ultrasonic attenuation and propagation speed in mammalian tissues as a function of temperature," Ultrasound Medicine Biol. **5**(2), 149–157 (1979).
48. R. O. Esenaliev, "Optoacoustic monitoring of physiologic variables," Front. Physiol. **8**, 1030 (2017).
49. B. Marty, B. Larrat, M. Van Landeghern, C. Robic, P. Robert, M. Port, D. Le Bihan, M. Pernot, M. Tanter, F. Lethimonnier, and S. Meriaux, "Dynamic study of blood-brain barrier closure after its disruption using ultrasound: a quantitative analysis," J. Cereb. Blood Flow Metab. **32**(10), 1948–1958 (2012).
50. O. Couture, J. Foley, N. F. Kassell, B. Larrat, and J.-F. Aubry, "Review of ultrasound mediated drug delivery for cancer treatment: updates from pre-clinical studies," Translational Cancer Research **3**, 494–511 (2014).
51. S. B. Raymond, L. H. Treat, J. D. Dewey, N. J. McDannold, K. Hynynen, and B. J. Bacskai, "Ultrasound enhanced delivery of molecular imaging and therapeutic agents in Alzheimer's disease mouse models," PLoS One **3**(5), e2175 (2008).
52. V. L. Tran, A. Novell, N. Tournier, M. Gerstenmayer, A. Schweitzer-Chaput, C. Mateos, B. Jego, A. Bouleau, H. Nozach, A. Winkeler, B. Kuhnast, B. Larrat, and C. Truillet, "Impact of blood-brain barrier permeabilization induced by ultrasound associated to microbubbles on the brain delivery and kinetics of cetuximab: An immunopet study using 89zr-cetuximab," J. Controlled Release **328**, 304–312 (2020).
53. D. G. Fisher and R. J. Price, "Recent advances in the use of focused ultrasound for magnetic resonance image-guided therapeutic nanoparticle delivery to the central nervous system," Front. Pharmacol. **10**, 1348 (2019).
54. B. Larrat, M. Pernot, J.-F. Aubry, E. Dervishi, R. Sinkus, D. Seilhean, Y. Marie, A.-L. Boch, M. Fink, and M. Tanter, "MR-guided transcranial brain HIFU in small animal models," Phys. Med. Biol. **55**(2), 365–388 (2010).
55. M. Gerstenmayer, "Ultrasound induced blood-brain barrier opening on rodents: from nanoparticles delivery to a therapy for Alzheimer's disease," Ph.D. thesis, University Paris-Saclay (ComUE) (2018).
56. Q. Zhou, K. H. Lam, H. Zheng, W. Qiu, and K. K. Shung, "Piezoelectric single crystal ultrasonic transducers for biomedical applications," Prog. Mater. Sci. **66**, 87–111 (2014).
57. R. Nasoni, T. Bowen, W. Connor, and R. Sholes, "In vivo temperature dependence of ultrasound speed in tissue and its application to noninvasive temperature monitoring," Ultrason. Imaging **1**(1), 34–43 (1979).
58. F. Zhang, G. Hao, M. Shao, K. Nham, Y. An, Q. Wang, Y. Zhu, C. M. Kusminski, G. Hassan, R. K. Gupta, Q. Zhai, X. Sun, P. E. Scherer, and O. K. Oz, "An Adipose tissue atlas: an image-guided identification of human-like BAT and beige depots in rodents," Cell Metab. **27**(1), 252–262.e3 (2018).
59. Y. Wang, D. Xing, Y. Zeng, and Q. Chen, "Photoacoustic imaging with deconvolution algorithm," Phys. Med. Biol. **49**(14), 3117–3124 (2004).
60. N. Nizam-Uddin and I. Elshafiey, "Enhanced energy localization in hyperthermia treatment based on hybrid electromagnetic and ultrasonic system: proof of concept with numerical simulations," Biomed Research International **2017**, 5787484 (2017).